Cryogenian interglacial greenhouse driven by enhanced volcanism: Evidence from mercury records

Ting Zhou [a,b], Xin Pan [a,b], Ruiyang Sun [a,b], Changzhou Deng [a], Jun Shen [c], Sae Yun Kwon [d], Stephen E. Grasby [e], Jiafei Xiao [a,*], Runsheng Yin [a,*]

[a] *State Key Laboratory of Ore Deposit Geochemistry, Institute of Geochemistry, Chinese Academy of Sciences, Guiyang, 550002, China*
[b] *University of Chinese Academy of Sciences, Beijing 100049, China*
[c] *State Key Laboratory of Geological Processes and Mineral Resources, China University of Geosciences, Wuhan, 430074, China*
[d] *Division of Environmental Science and Engineering, Pohang University of Science and Technology, 77 Cheongam-Ro, Nam Gu, Pohang 37673, South Korea*
[e] *Geological Survey of Canada, Calgary Natural Resources Canada, 3303 33rd Street NW, Calgary, AB, T2L 2A7, Canada*

ARTICLE INFO

ABSTRACT

An ice-free greenhouse interval (ca. 660 ∼ 650 Ma) occurred between the global Sturtian (ca. 717 Ma ∼ 660 Ma) and Marinoan glaciation (ca. 650 Ma ∼ 635 Ma) during the Cryogenian. While volcanic CO_2 emissions have been suggested as a trigger for this ice-free interval, evidence for volcanism has been lacking. In this study, spikes in both Hg concentration (76 to 366 ppb) and Hg to total organic carbon ratio (Hg/TOC: 114 to 717 ppb/wt.%) were observed in the Wuhe section of South China, suggesting that extensive volcanic emissions of Hg occurred during the Cryogenian interglacial period. Positive $\Delta^{199}Hg$ (0.02 to 0.18‰) values were observed in these Hg-rich shales, indicating that the volcanic Hg was cycling in the atmosphere, deposited in seawater, and sequestered to sediment via organic matter burial. Combined with other geochemical proxies (e.g., organic carbon isotope and chemical index of alteration), our results provide the first direct evidence that volcanism played a key role in forming the brief Cryogenian interglacial period.

1. Introduction

The Neoproterozoic era (1000-541 Ma), marked by the Rodinia supercontinent breakup, low latitude glaciation, and biotic diversification, is a critical time in Earth's evolution (Li et al., 2008; Hoffman et al., 2017). Perhaps the most dramatic of all were events during the Cryogenian, when the planet was largely covered by ice during the Sturtian glaciation (ca. 717 Ma∼660 Ma) and Marinoan glaciation (ca. 650 Ma∼635 Ma). Equally dramatic was the ice-free interglacial interval (ca. 660∼650 Ma), representing a relatively brief repose from global ice cover (Hoffman et al., 2017; Bao et al., 2018). Widespread black shale deposition during this interglacial period (e.g. southern China, Canada, Oman, Australia), suggests significant changes occurred in environmental conditions, including a global climate shift to greenhouse conditions (Hoffman et al., 2017). Although the chronology and ocean redox state of this unique interglacial interval have been studied extensively (Li et al., 2012; Zhou et al., 2019), the mechanism driving the climate shift from icehouse to greenhouse remains a mystery. The Ongeluk large igneous province (LIP) (2426 ± 3 Ma) was suggested to have ended the earlier Paleoproterozoic glaciation through the release of massive amounts of CO_2 reestablishing a greenhouse atmosphere (Ernst and Youbi, 2017; Gumsley et al., 2017). However, evidence for such eruptions during the Cryogenian is lacking due to the inherent difficulty of preserving datable ash beds in an ice-covered world. As such, other geochemical fingerprints of volcanism need interigation to test for potential LIP-driven warming in the Cryogenian.

Mercury (Hg), is a globally distributed volatile trace metal that can be used to fingerprint LIP events (Sanei et al., 2011; Grasby et al., 2017, 2019; Shen et al., 2020), providing direct temporal control on the timing of volcanism relative to the impacts on global biogeochemical cycles it is thought to drive, as recorded in the sedimentary record. Volcanoes emit large amounts of gaseous (Hg^0) to the atmosphere. Hg^0 has an atmospheric lifetime of ∼1 year, allowing its global interhemispheric distribution prior to deposition onto land and oceans (Selin, 2009). As organic matter (OM) has a strong affinity to Hg, OM drawdown shuttles Hg to the seafloor. The ultimate sink of Hg is burial and sequestration in ocean sediments (Grasby et al., 2020). Over most of geological

history, volcanic Hg emissions appear balanced by this OM shuttle (Grasby et al., 2013). However, transient Hg emission events, related to Large Igneous Provinces (LIPs) eruptions are documented throughout the Phanerozoic (Sanei et al., 2011; Grasby et al., 2017, 2019, 2020), causing significantly high Hg/TOC ratios that are recorded as Hg spikes in the sediment record (Grasby et al., 2020). Such Hg spikes have been suggested as a proxy for extensive Hg emissions from LIPs (Grasby et al., 2019).

Hg isotope ratios further serve as a powerful proxy for understanding the sources and fates of Hg in the environment (Kwon et al., 2020). Hg isotopes undergo both mass-dependent fractionation (MDF, presented as δ^{202}Hg) and mass-independent fractionation (MIF, presented as Δ^{199}Hg). Hg-MDF is ubiquitous and occurs via physical, chemical, and biological processes. Hg-MIF occurs primarily during photochemical processes with little influence via other environmentally relevant processes. Thus, Hg-MIF provides relatively conservative and precise information regarding Hg sources (Blum et al., 2014). Volcanic Hg has shown small Hg-MIF signals (with Δ^{199}Hg of at least ∼0.05‰) that can be created by evaporation during magmatic degassing (Moynier et al., 2020). However, once emitted into the atmosphere, Hg(II) photoreduction process can cause Hg-MIF, leading to positive Δ^{199}Hg in marine systems (e.g., seawater and marine sediments) and negative Δ^{199}Hg in terrestrial systems (e.g., soil and vegetation) (Blum et al., 2014). Hg stable isotopes have also proven useful to identify sources of Hg spikes found at the boundaries of the "Big Five" mass extinctions as well as several oceanic anoxia events through the Phanerozoic, highlighting the importance of LIPs as drivers of these events (Grasby et al., 2019; Shen et al., 2020). Hg records in the Neoproterozoic era have rarely been reported, however.

Sedimentary records of the Sturtian and Marinoan glaciations are well preserved in the Nanhua Basin of south China. Black shales, which are typically rich in Hg, were widely deposited in the Nanhua Basin in the aftermath of the Sturtian glaciation (Li et al., 2012). The Wuhe section, South China, preserves an integrated record of the Datangpo Formation during the interglacial period between the Sturtian and Marinoan glaciations. Hg concentrations, major and trace elements, total organic carbon content (TOC), Hg and carbon isotopic composition analyses were performed in this study to test the hypothesis that volcanism at the onset of the Cryogenian was responsible for the inter-glacial interval.

2. Geological background

The Nanhua Rift Basin was developed between the Yangtze and Cathaysia blocks, during the break-up of the supercontinent Rodinia (Wang and Li, 2003). Neoproterozoic sedimentary rocks spanning from Tonian to Ediacaran were deposited in this basin (Fig. 1). The widely occurring Cryogenian deposits become thicker from northwest to southeast, transitioning from shallow-water platform to slope and basinal facies (Jiang et al., 2003; Zhou et al., 2019). The Wuhe section is located in southeastern Guizhou Province, South China, an area representing slope/basinal facies (Jiang et al., 2003). Cryogenian successions in this location comprise the glacial Tiesi'ao and Nantuo formations, which are commonly identified to be the stratigraphic equivalents of other Sturtian and Marinoan glacial units elsewhere, respectively (Zhang et al., 2003). The Datangpo Formation, occurring conformably in between the Tiesi'ao and Nantuo formations, is considered a non-glacial marine sedimentary deposit representing ∼10 Ma of deposition (Bao et al., 2018).

In the Wuhe section, the glacial Tiesi'ao Formation and Nantuo Formation are represented by a ∼4 m-thick grey diamictite and a ∼150 m-thick massive or stratified diamictite, respectively. The intervening non-glacial Datangpo Formation can be divided into three lithological members (Fig. 2): Member I consists of ∼0.3 m
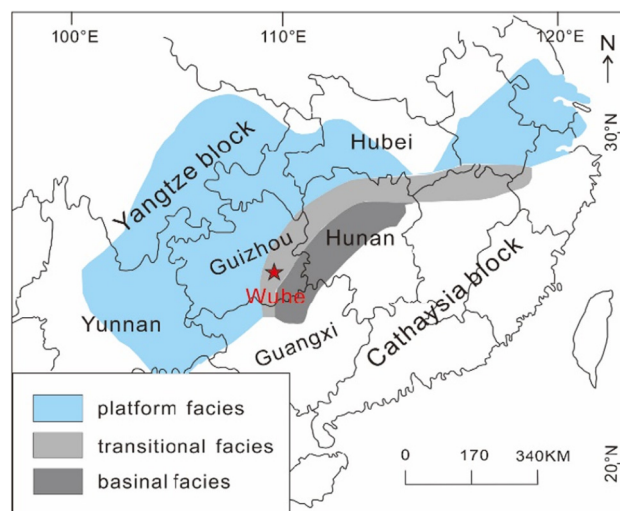

Fig. 1. Geographic map of South China in the Cryogenian interglacial interval and location the studied Wuhe section (modified after Jiang et al. (2003) and Zhou et al. (2019)).

Mn-bearing dolomite and ∼0.2 m grey siltstone. Member II consists of ∼8 m of organic-rich black shales. Member III consists of ∼60 m light-green shales.

3. Methods

Fresh rock samples were collected from the Wuhe section (Fig. 2). A detailed description of the samples can be found in Table S1. In the laboratory, any remaining weathered surfaces were removed. For the diamictites in the Tiesi'ao Formation, fine-grained components were sampled from sliced sample pieces using a handheld drill. Any pebbles or large-sized clasts in diamictites were not drilled. The black shale samples were washed by 18.2 MΩ·cm water and air-dried. All the samples were powdered to ∼200 mesh in an agate mortar, and homogenized prior to chemical analyses at the Institute of Geochemistry, Chinese Academy of Sciences (IGCAS).

Analyses of major elements were conducted using an ARL Perform' X 4200 XRF, with an analytical uncertainty of <5%. Concentrations of trace elements were analyzed using a Plasma Quant-MS Elite ICP-MS, following methods of (Liang et al., 2000). Rock standard reference material (SRM) AGV-2 was measured for quality assurance, which yielded an average recovery of 90% (n = 3) and reproducibility of < 10% for all trace elements measured in this study.

For TOC and TS analyses, sample powders were first leached using 2.5 N HCl to remove possible inorganic carbon. The residual powder was then rinsed with 18.2 MΩ·cm water, freeze-dried, and measured using an Elementar various micro cube analyzer with analytical errors <2.5%. For organic carbon isotope analyses, samples were de-carbonated with 2.5 N HCl for 12 h. After freeze-drying, the organic carbon isotope compositions were measured using a MAT253 Stable Isotope Ratio Mass Spectrometer, with an analytical uncertainty of ∼0.2‰ during the analysis. Isotope results are reported in conventional $\delta^{13}C_{org}$ notation, defined as per mil (‰) deviation from the Vienna Pee Dee Belemnite (VPDB).

Mercury concentration was measured using a DMA-80 mercury analyzer, which yielded Hg recovery of 95% (n = 4) and reproducibility of < 10% for SRM GSS-5. For Hg isotope ratios, Hg in the samples was first preconcentrated in 5 mL 40% versa aqua regia (HCl/HNO$_3$ = 1/3, v/v) using a dual-stage combustion furnace (Zerkle et al., 2020). This method yielded an average Hg recovery of 90% for SRM BCR-482. The preconcentrated solutions were
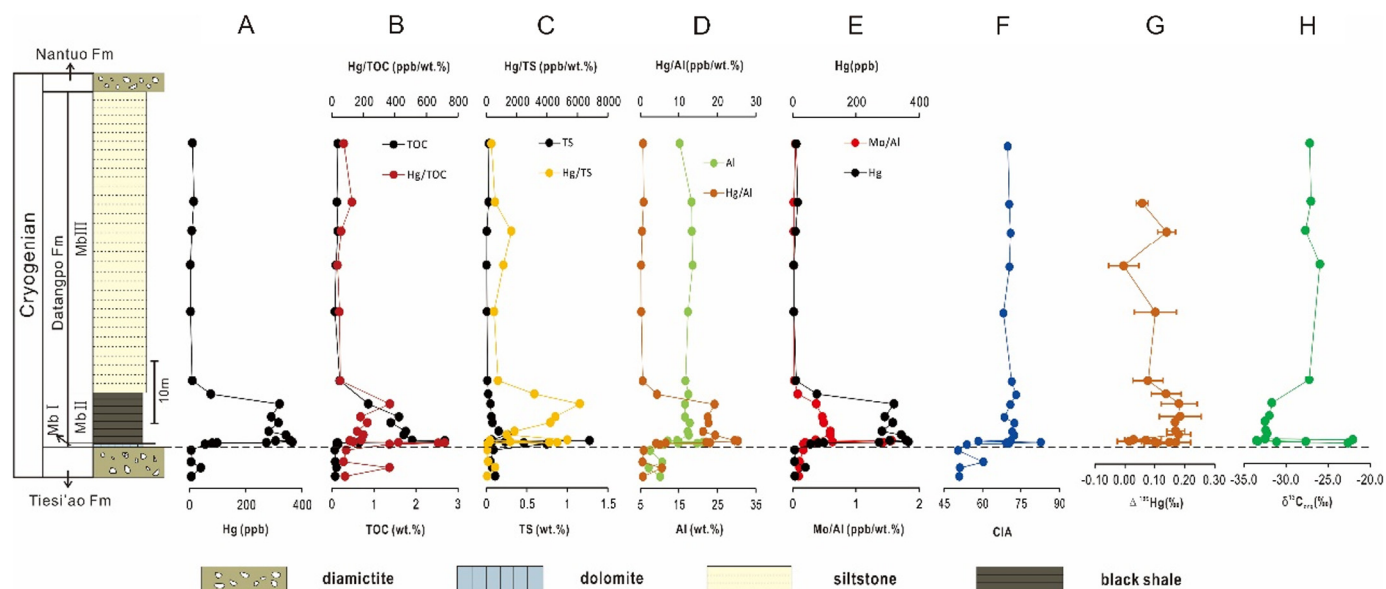
Fig. 2. (A) Hg concentrations; (B) TOC contents and Hg/TOC ratios; (C) TS contents and Hg/TS ratios; (D) Al contents and Hg/Al ratios; (E) Hg contents and Mo/Al ratios; (F) chemical index of alteration values (CIA); (G) Δ^{199}Hg values; and (H) $\delta^{13}C_{org}$ values of studied samples. (For interpretation of the colors in the figure(s), the reader is referred to the web version of this article.)

diluted to 0.5 ng/mL Hg, with an acidity of ~10%, and measured using a Neptune Plus MC-ICP-MS, following a method by (Yin et al., 2016). As recommended by (Bergquist and Blum, 2007), MDF of Hg isotopes is expressed in δ^{202}Hg notation in units of per mil (‰) referenced to the NIST-3133 Hg standard:

$$\delta^{202}Hg = [(^{202}Hg/^{198}Hg_{sample})/(^{202}Hg/^{198}Hg_{standard}) - 1] \times 1000 \quad (1)$$

Mass independent fractionation of Hg isotopes is reported in Δ notation:

$$\Delta^{199}Hg \approx \delta^{199}Hg - \delta^{202}Hg \times 0.2520 \quad (2)$$

$$\Delta^{200}Hg \approx \delta^{200}Hg - \delta^{202}Hg \times 0.5024 \quad (3)$$

$$\Delta^{201}Hg \approx \delta^{201}Hg - \delta^{202}Hg \times 0.7520 \quad (4)$$

Analytical uncertainty was estimated based on the replicates of the NIST 3177 secondary standard solution and full procedural analyses of BCR-482. The overall average and uncertainty of NIST-3177 (δ^{202}Hg: -0.53 ± 0.10‰; Δ^{199}Hg: 0.02 ± 0.08‰; Δ^{201}Hg: 0.03 ± 0.07 ‰; 2SD, n=11) and BCR-482 (δ^{202}Hg: -1.53±0.10‰; Δ^{199}Hg: -0.61±0.08‰; Δ^{201}Hg: -0.62±0.06‰; 2SD, n=4) agree well previous results (Blum and Bergquist, 2007; Estrade et al., 2010). Uncertainties reported in this study correspond to the larger value of either (1) the measurement uncertainty of replicate digests of BCR-482, or (2) the uncertainty of repeated measurements of NIST-3177.

4. Results

Major and trace element concentrations, Hg concentrations and isotope ratios, TOC, and organic carbon isotope ratios of the samples are summarized in Tables S1 and S2 and illustrated in Fig. 2. In the glacial Tiesi'ao Formation, the diamictite samples have low Hg concentrations of ~6 ppb. The TOC and TS contents in these samples are also low (<0.10 wt.%). The Hg/TOC and Hg/TS ratios range from 74 to 366 ppb/wt.% and 61 to 575 ppb/wt.%, respectively, although may not be considered reliable given the low TOC values (Grasby et al., 2019). Due to the low Hg concentrations, the

Hg isotopic composition of the Tiesi'ao Formation was not measured.

The inter-glacial Datangpo Formation has geochemical signals that are distinct from the Tiesi'ao Formation. The dolomite and siltstone samples in Member I show much higher Hg concentrations of 55 and 81 ppb, with δ^{202}Hg of -0.90 to -1.14‰ and Δ^{199}Hg of 0.10 to 0.17‰, respectively. TOC contents in these samples are still low (<0.2%), with $\delta^{13}C_{org}$ of -31.1 to -22.65‰. The Hg/TOC values in Member I are the highest, ranging from 366 to 675 ppb/%, but again unreliable. The Hg/TS values are in general low, ranging from 75 to 174 ppb/wt.%.

The black shale samples in Member II have high Hg concentrations (76 to 366 ppb) that all exceed average shale values of 64.2 ppb (Grasby et al., 2019). Most of the samples show TOC contents of >0.2 wt.% and as high as 2.69 wt.%. The upper part of Member II had Δ^{199}Hg values of 0.14 to 0.18‰, similar to Member I except for three samples located at the lower part, which had near-zero Δ^{199}Hg (0.02 to 0.07‰). The δ^{202}Hg values are around -1.8‰ for most samples. The majority of black shales showed $\delta^{13}C_{org}$ values of -33.5 to -31.7‰. Member II showed intermediate Hg/TOC values, ranging from 114 to 717 ppb/wt.% although the highest ratio is 423 ppb/wt.% when excluding the lowest TOC values from this calculation. The highest Hg/TS values (240 to 6166 ppb/wt.%) were found in this member.

The siltstone samples in Member III showed the lowest Hg concentrations (3.4 to 15.3 ppb) and TOC contents (<0.2 wt.%), compared to Members I and II. Compared to Member II, relatively lower Δ^{199}Hg (0.00 to 0.14‰) and relatively higher δ^{202}Hg and $\delta^{13}C_{org}$ (-0.82 to -0.51‰ and -27.7 to -26.0‰ respectively) were observed. The Hg/TOC ratios (36 to 128 ppb/wt.%) were the lowest compared to Member I and II and are again unreliable at these low TOC values, and the Hg/TS ratios were 333 to 1643 ppb/wt.%.

The glacial samples show low chemical index of alteration (CIA) values ranging from 50~60. In contrast, the CIA of inter-glacial samples shows constant values of ~70. Meanwhile, peaks of Hg/Al (4.1~25.4) and Mo/Al (0.08~1.56) are observed in Member I and II.
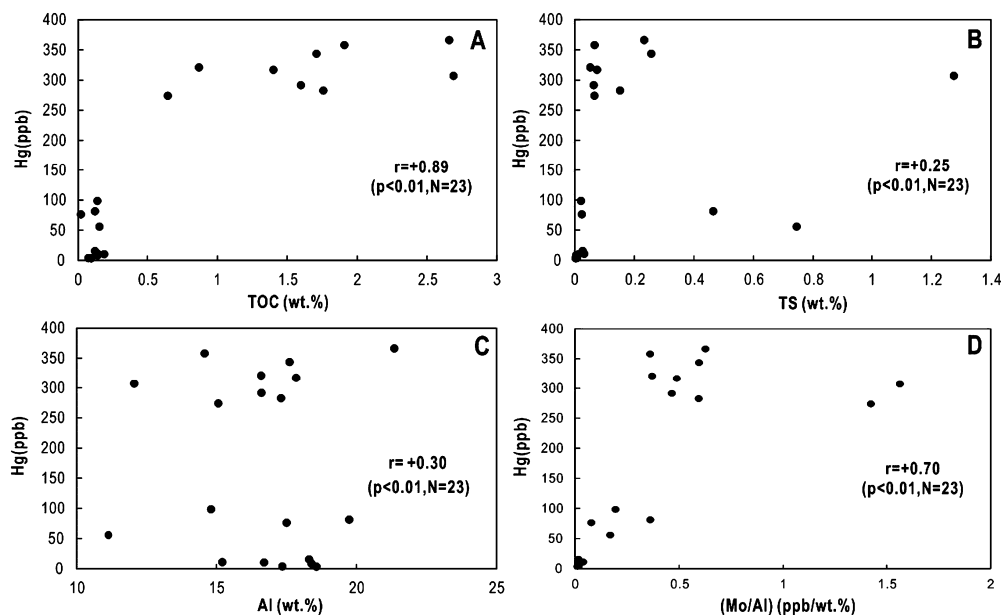
Fig. 3. Correlations between: (A) TOC and Hg; (B) TS and Hg; (C) Al and Hg; and (D) Mo/Al and Hg.

5. Discussion

5.1. Understanding the host phases of Hg in the Datangpo formation

The host phases of Hg must be investigated to understand the peaks of Hg concentration in Member I and Member II. The main phases hosting Hg in sediments are organic matter, sulfides, and clay minerals (Ravichandran, 2004; Selin, 2009; Sanei et al., 2011; Grasby et al., 2019; Shen et al., 2019, 2020). Organic matter has a high affinity to Hg due to the formation of Hg-OM complexes (Ravichandran, 2004), and organic burial serves as a dominant control on Hg deposition to the seafloor (Grasby et al., 2015). Under anoxic and euxinic conditions, however, Hg can form complexes with reduced sulfur species due to the high stability constants of the Hg-S complexes, leading to extreme enrichment of Hg in sulfides (e.g. pyrite) (Sanei et al., 2011; Shen et al., 2019, 2020). Clay minerals can also absorb substantial amounts of Hg due to their high surface area to volume ratio (Grasby et al., 2019). The correlations between Hg and TOC, TS, and Al contents were used to assess the main host phase of Hg in previous studies (Shen et al., 2019, 2020). In our study, a significantly positive correlation was observed between Hg and TOC concentrations (Fig. 3A, r = 0.89). In contrast, we did not observe significant correlations between TS and Hg contents (Fig. 3B, r= 0.25) and between Al and Hg (Fig. 2D and Fig. 3C, r = 0.30). This suggests that Hg is mainly hosted by organic matter. In layers where TOC is very low (<0.2 wt.%) Hg is also very low and as such this does not affect our focus on the layers with anomalously high Hg concentrations.

Increased sedimentation rates can decrease Hg contents in the sediment via dilution of imported materials (Percival et al., 2015). Reduction in sedimentation rates may lead to the Hg peaks observed in our study. According to the latest astrochronology study (Bao et al., 2018); however, the average sedimentation rate during the Cryogenian interglacial (∼10 Ma) is estimated to be ∼7 m/Myr based on the total thickness of the Datangpo Formation (∼70 m) at Wuhe. This high sedimentation rate is much higher than those reported in other successions, in which Hg enrichments are found (Wang et al., 2018). Percival et al. (2015) estimated that a ∼5- to 10-fold reduction in sedimentation rate is needed to generate a measurable Hg enrichment, which is not what we observed in this study. Therefore, changes in the sedimentation rates may not explain the temporal variations in Hg.

Previous studies also suggested that sediment deposited under euxinic conditions can generate Hg anomalies by forming Hg-S complexes in the water column without external Hg input (Gehrke et al., 2009; Sanei et al., 2011; Shen et al., 2019). The anomalously high Hg/TS ratios observed in Member II samples indicate enrichment of Hg relative to sulfur (Fig. 2C) where most samples were deposited under dysoxic to slightly anoxic conditions (Fig. S1). As such S drawdown under euxinic conditions can be excluded as a cause of Hg enrichment.

Changes in redox conditions can also affect Hg accumulation in sediments (Gehrke et al., 2009). Oxygen deficient conditions were widespread in oceans during the Proterozoic era (Lyons et al., 2009). In this study, the redox indicator Mo/Al (Algeo and Maynard, 2004), and Hg concentrations showed significantly positive correlations (Figs. 2E, 3D, r = 0.70), suggesting that increased Hg levels were possibly driven by enhanced anoxic conditions. Under anoxic conditions, organic matter burial is promoted and therefore greater amounts of Hg can be removed from the water column (Grasby et al., 2019), although this would not change the Hg/TOC ratios, and without increased Hg availability this would lead to eventual Hg depletion in the water column.

5.2. Hg anomalies indicate major volcanism drove the Cryogenian greenhouse

Volcanic emissions are the main natural source of Hg in the global environment, and periods of significant volcanic activity can lead to enhanced Hg deposition to world oceans and subsequent sequestration into sediments on a millennial timescale (Sanei et al., 2011; Grasby et al., 2019, 2020). When other factors are ruled out, anomalous Hg concentrations and Hg/TOC spikes can thus be used as a proxy of extensive volcanic Hg emissions (Grasby et al., 2019), and have been observed in sediments deposited during a large number of environmental perturbation events throughout geological history that were driven by LIP events (Sanei et al., 2011; Percival et al., 2015; Grasby et al., 2019; Percival et al., 2021; Shen et al., 2020). Consistent with this, we interpret that the high Hg concentrations together with Hg/TOC ratios in Members I and II (Figs. 2A and 2B) suggest the presence of extensive volcanic Hg emission at the onset of the Cryogenian interglacial interval. The samples in Member I and II have Hg concentrations ranging between 50 and 366 ppb and Hg/TOC ratios ranging between 114

and 717 ppb/wt.%, which are comparable with those of the sediment records perturbed by large-scale volcanic activities (Grasby et al., 2015, 2019).

According to Grasby et al. (2019), unreliable Hg/TOC could appear when Hg concentrations are normalized to TOC values of <0.2% due to increasing analytical uncertainties. For samples in Member I, the TOC contents were lower than 0.2%, indicating that the Hg/TOC ratios are likely unreliable. However, this also means that Hg concentrations (50 to 81 ppb) were not influenced by changes in organic matter drawdown, such that the significant increase in Hg compared to the underlying Tiesi'ao Formation likely reflects enhanced Hg loading to the environment. In Member II, high TOC contents (up to 2.69%) indicate increased OM burial. These black shales also showed high Hg concentrations (76 to 366 ppb) and high Hg/TOC ratios (>200 ppb/%), suggesting again enhanced Hg loading to the environment (Figs. 2A and 2B).

Mercury isotopes can provide more precise constraints on the Hg source. In this study, δ^{202}Hg varied from -0.90‰ to-1.14‰ in Member I, -1.97 to -0.48‰ in Member II, and -0.82‰ to -0.51‰ in Member III (Table S2), suggesting either changes in Hg sources or biogeochemical processes are required to explain changes in Hg-MDF. However, as mentioned above, MDF occurs during a large number of physical, chemical, and biological processes (Blum et al., 2014). Since we lack a complete understanding of these processes, it is difficult to discuss δ^{202}Hg further here.

Hg-MIF is caused primarily via photochemical reactions (Blum et al., 2014), therefore, it can provide more clear constraints on the Hg sources compared to δ^{202}Hg. Mercury emitted by volcanic activity is characterized by small Hg-MIF signals, with Δ^{199}Hg of at least ∼0.05‰ (Moynier et al., 2020). However, once released to the environment, Hg undergoes complex cycling in the land-ocean-atmosphere system. Photo-reduction of Hg in aquatic ecosystems (e.g., ocean and lakes) and cloud droplets can lead to a lower Δ^{199}Hg in the gaseous Hg(0) and a higher Δ^{199}Hg in the residual Hg(II) pool. As a result, it has been suggested that seawater has a positive Δ^{199}Hg due to the wet deposition of Hg(II) (Štrok et al., 2015), and terrestrial soil and vegetation are characterized by negative Δ^{199}Hg due to the accumulation of Hg(0) (Yin et al., 2013). For this reason, coastal sediments, which receive Hg from riverine and terrestrial runoff, have been characterized by negative to zero Δ^{199}Hg (-0.3 to 0‰), and marine sediments have shown positive Δ^{199}Hg due to the deposition of atmospherically sourced and seawater Hg through OM drawdown (0 to 0.4‰) (Yin et al., 2015; Grasby et al., 2017). The interglacial Datangpo Formation was deposited under a slope/basin environment and exhibits positive Δ^{199}Hg values associated with high Hg concentrations (Fig. 2G). Together with the high Hg/TOC ratios, we suggest that Hg emitted from extensive volcanic activities has undergone photo-reduction in the atmosphere and surface water, which was then deposited to the sediment via the scavenging of OM from the water column. This resulted in the preservation of the positive Δ^{199}Hg values in marine sediments.

Extensive volcanic activity, such as LIP and continental arc volcanos, not only emitted large amounts of CO_2 that drives global warming, but also large volumes of volcanic rocks, which both play important roles in governing Earth climate (Ernst, 2014; Lee et al., 2015; Cao et al., 2017). We note the temporal correspondence between the negative shifts in $\delta^{13}C_{org}$ (magnitude of ∼ 5‰) (Fig. 2H) with Hg concentration, Hg/TOC, and Δ^{199}Hg anomalies (Figs. 2A, 2B, 2G). If our interpretation is correct, then these Hg anomalies reflect enhanced volcanic activity, and we propose that associated lava discharge had a profound impact on the carbon cycle during this period by releasing massive amounts of ^{13}C depleted CO_2 and methane, as suggested by some previous studies (Shen et al., 2012; Gutjahr et al., 2017). Abruptly increased CIA values (∼70) in the Datangpo Formation (Fig. 2F), relative to those of the underlying

fresh diamictites (50∼60), indicate enhanced silicate weathering during the interglacial periods, which is probably due to the warming effects brought by volcanism (Nesbitt and Young, 1982). Our increased CIA data is consistent with many other Cryogenian interglacial records across south China and other parts of the world (e.g. Congo, Australia) (Wang et al. (2020) and references therein).

While the surface of Earth was frozen during the Cryogenian glaciations, plate tectonics and magmatism stayed uninterrupted. Recent studies show that the intensity of global continental arc activities enhanced (e.g. increased arc lengths) during the middle to late Cryogenian periods (McKenzie et al., 2016; Cao et al., 2017). LIP and rifting activity associated with the prolonged break-up of the Rodinia super-continent were likely to be also active during the interglacial period (Ernst et al., 2008; Li et al., 2008). After its complete assembly, a mantle super-plume was formed beneath Rodinia, which finally led to its break-up. As a result, prolonged and periodic plume activity (mainly from ca. 900 Ma∼700 Ma) occurred (Ernst et al., 2008). A recent study discovered abundant mafic-ultra mafic dike swarms of ca. 700 Ma∼650 Ma along the northern margin of the Yangtze Block (Zhao et al. (2018) and references therein), which could be considered as a causative LIP event. To date, evidence for volcanic activity during the preceding Sturtia glaciation remains rare. However, the large Hg peaks observed in this study certainly support large volcanism at the onset of the Cryogenian inter-glacial interval. These volcanic activities could release CO_2, heating the Earth's surface, and thus played an important role in ending the Cryogenian glaciation. As shown in Fig. 4, we propose the following scenarios for the Cryogenian interglacial interval: (1) At the end of the Sturtian glaciation (Fig. 4A), extensive volcanic activity released large amounts of lava, in addition to releasing atmospheric Hg and CO_2 through both eruptions and thermogenic processes (Svensen et al., 2018; Jones et al., 2019). The large amount of CO_2 and other greenhouse gases resulted in global warming, which played an important role in ending the Sturtian glaciation; (2) During the Cryogenian inter-glacial interval (Fig. 4B), global warming led to enhanced silicate weathering and enhanced input of nutrients to the ocean, leading to enhanced ocean productivity and burial of high amounts of OM (as well as high seawater Hg deposition) onto the seafloor, indicated by the formation of Hg-rich black shales in Member II. (3) At the end of the Cryogenian interglacial interval (Fig. 4C), extensive volcanic activity waned, but silicate weathering continued (as suggested by the increased CIA values), which gradually exhausted the atmospheric CO_2 and other greenhouse gases, driving global cooling and onset of the subsequent Marinoan glaciation. During this process, Hg deposited into the ocean decreased significantly due to the reduction in external Hg supply, as evidenced by the low Hg concentration and low Hg/TOC ratios in Member III.

6. Conclusion

Through investigation of Hg concentration and isotopic composition, and other geochemical proxies ($\delta^{13}C_{org}$ and CIA) in the Wuhe section, our study demonstrates that extensive volcanic activity occurred at the end of the Sturtian glaciation. Extensive volcanic activity not only emitted massive amounts of volcanic rocks onto the Earth's surface, but also released large amounts of CO_2 and Hg into the atmosphere. High atmospheric CO_2 levels resulted in global warming that played an important role in the termination of the Sturtian glaciation and the occurrence of the Cryogenian inter-glacial greenhouse. Global warming enhanced silicate weathering and ocean productivity, thereby leading to the deposition of Hg-rich black shales onto the seafloor. The extensive volcanic activity stopped at the later stage of the Cryogenian interglacial interval, during which the massive amount of previously emitted
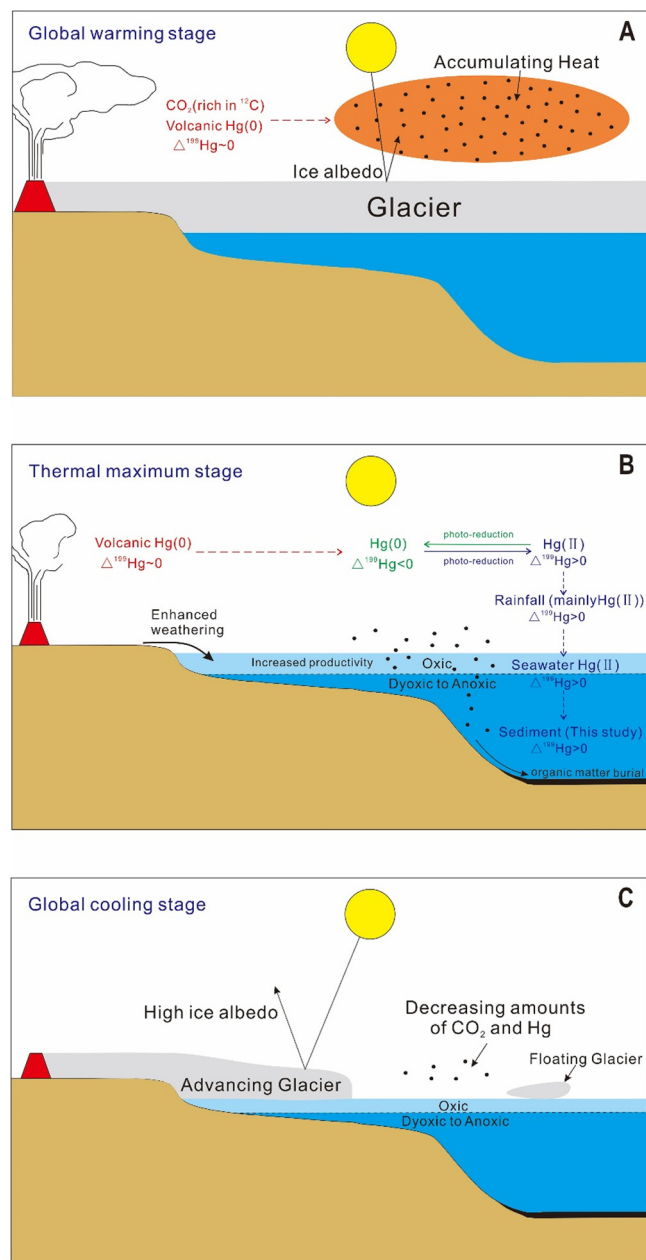
Fig. 4. Scenarios of Hg biogeochemical cycling during: (A) Early Cryogenian interglacial interval; (B) Middle Cryogenian interglacial interval; and (C) Late Cryogenian interglacial interval.

volcanic rocks continued to exhaust atmospheric CO_2, leading to the deposition of low Hg sediments and the occurrence of Marinoan glaciation. This study thus provides important information regarding the linkage between large igneous province volcanism and climate change during early Earth.

CRediT authorship contribution statement

Ting Zhou: Conceptualization, Investigation, Writing – original draft. **Xin Pan:** Data curation, Investigation. **Ruiyang Sun:** Data curation, Investigation. **Changzhou Deng:** Data curation, Investigation. **Jun Shen:** Writing – review & editing. **Sae Yun Kwon:** Writing – review & editing. **Stephen E. Grasby:** Writing – review & editing. **Jiafei Xiao:** Supervision. **Runsheng Yin:** Conceptualization, Methodology, Supervision.

Declaration of competing interest

The authors declare that they have no known competing financial interestsor personal relationships that could have appeared to influence the work reported in this paper.

Appendix A. Supplementary material

Supplementary material related to this article can be found online at https://doi.org/10.1016/j.epsl.2021.116902.

References

Algeo, T.J., Maynard, J.B., 2004. Trace-element behavior and redox facies in core shales of Upper Pennsylvanian Kansas-type cyclothems. Chem. Geol. 206, 289–318.

Bao, X., Zhang, S., Jiang, G., Wu, H., Li, H., Wang, X., An, Z., Yang, T., 2018. Cyclostratigraphic constraints on the duration of the Datangpo formation and the onset age of the Nantuo (Marinoan) glaciation in South China. Earth Planet. Sci. Lett. 483, 52–63.

Bergquist, B.A., Blum, J.D., 2007. Mass-dependent and -independent fractionation of Hg isotopes by photoreduction in aquatic systems. Science 318, 417–420.

Blum, J.D., Bergquist, B.A., 2007. Reporting of variations in the natural isotopic composition of mercury. Anal. Bioanal. Chem. 388, 353–359.

Blum, J.D., Sherman, L.S., Johnson, M.W., 2014. Mercury isotopes in Earth and environmental sciences. Annu. Rev. Earth Planet. Sci. 42, 249–269.

Cao, W., Lee, C.-T.A., Lackey, J.S., 2017. Episodic nature of continental arc activity since 750 Ma: a global compilation. Earth Planet. Sci. Lett. 461, 85–95.

Ernst, R., Wingate, M., Buchan, K., Li, Z.-X., 2008. Global record of 1600–700 Ma Large Igneous Provinces (LIPs): implications for the reconstruction of the proposed Nuna (Columbia) and Rodinia supercontinents. Precambrian Res. 160, 159–178.

Ernst, R.E., 2014. Large Igneous Provinces. Cambridge University Press.

Ernst, R.E., Youbi, N., 2017. How Large Igneous Provinces affect global climate, sometimes cause mass extinctions, and represent natural markers in the geological record. Palaeogeogr. Palaeoclimatol. Palaeoecol. 478, 30–52.

Estrade, N., Carignan, J., Sonke, J.E., Donard, O.F., 2010. Measuring Hg isotopes in bio-geo-environmental reference materials. Geostand. Geoanal. Res. 34, 79–93.

Gehrke, G.E., Blum, J.D., Meyers, P.A., 2009. The geochemical behavior and isotopic composition of Hg in a mid-Pleistocene western Mediterranean sapropel. Geochim. Cosmochim. Acta 73, 1651–1665.

Grasby, S.E., Beauchamp, B., Bond, D.P.G., Wignall, P.B., Sanei, H., 2015. Mercury anomalies associated with three extinction events (Capitanian Crisis, Latest Permian Extinction and the Smithian/Spathian Extinction) in NW Pangea. Geol. Mag. 153, 285–297.

Grasby, S.E., Liu, X., Yin, R., Ernst, R.E., Chen, Z., 2020. Toxic mercury pulses into late Permian terrestrial and marine environments. Geology 48, 830–833.

Grasby, S.E., Sanei, H., Beauchamp, B., Chen, Z., 2013. Mercury deposition through the Permo–Triassic Biotic Crisis. Chem. Geol. 351, 209–216.

Grasby, S.E., Shen, W., Yin, R., Gleason, J.D., Blum, J.D., Lepak, R.F., Hurley, J.P., Beauchamp, B., 2017. Isotopic signatures of mercury contamination in latest Permian oceans. Geology 45, 55–58.

Grasby, S.E., Them, T.R., Chen, Z., Yin, R., Ardakani, O.H., 2019. Mercury as a proxy for volcanic emissions in the geologic record. Earth-Sci. Rev. 196, 102880.

Gumsley, A.P., Chamberlain, K.R., Bleeker, W., Söderlund, U., de Kock, M.O., Larsson, E.R., Bekker, A., 2017. Timing and tempo of the great oxidation event. Proc. Natl. Acad. Sci. 114, 1811–1816.

Gutjahr, M., Ridgwell, A., Sexton, P.F., Anagnostou, E., Pearson, P.N., Pälike, H., Norris, R.D., Thomas, E., Foster, G.L., 2017. Very large release of mostly volcanic carbon during the Palaeocene–Eocene Thermal Maximum. Nature 548, 573–577.

Hoffman, P.F., Abbot, D.S., Ashkenazy, Y., Benn, D.I., Brocks, J.J., Cohen, P.A., Cox, G.M., Creveling, J.R., Donnadieu, Y., Erwin, D.H., 2017. Snowball Earth climate dynamics and Cryogenian geology-geobiology. Sci. Adv. 3, e1600983.

Jiang, G., Sohl, L.E., Christie-Blick, N., 2003. Neoproterozoic stratigraphic comparison of the Lesser Himalaya (India) and Yangtze block (south China): Paleogeographic implications. Geology 31, 917–920.

Jones, S.M., Hoggett, M., Greene, S.E., Jones, T.D., 2019. Large Igneous Province thermogenic greenhouse gas flux could have initiated Paleocene-Eocene Thermal Maximum climate change. Nat. Commun. 10, 1–16.

Kwon, S.Y., Blum, J.D., Yin, R., Tsui, M.T.-K., Yang, Y.H., Choi, J.W., 2020. Mercury stable isotopes for monitoring the effectiveness of the Minamata Convention on Mercury. Earth-Sci. Rev. 203, 103111.

Lee, C.-T.A., Thurner, S., Paterson, S., Cao, W., 2015. The rise and fall of continental arcs: interplays between magmatism, uplift, weathering, and climate. Earth Planet. Sci. Lett. 425, 105–119.

Li, C., Love, G.D., Lyons, T.W., Scott, C.T., Feng, L., Huang, J., Chang, H., Zhang, Q., Chu, X., 2012. Evidence for a redox stratified Cryogenian marine basin, Datangpo Formation, South China. Earth Planet. Sci. Lett. 331, 246–256.

Li, Z.-X., Bogdanova, S., Collins, A., Davidson, A., De Waele, B., Ernst, R., Fitzsimons, I., Fuck, R., Gladkochub, D., Jacobs, J., 2008. Assembly, configuration, and break-up history of Rodinia: a synthesis. Precambrian Res. 160, 179–210.

Liang, Q., Jing, H., Gregoire, D.C., 2000. Determination of trace elements in granites by inductively coupled plasma mass spectrometry. Talanta 51, 507–513.

Lyons, T.W., Anbar, A.D., Severmann, S., Scott, C., Gill, B.C., 2009. Tracking euxinia in the ancient ocean: a multiproxy perspective and Proterozoic case study. Annu. Rev. Earth Planet. Sci. 37, 507–534.

McKenzie, N.R., Horton, B.K., Loomis, S.E., Stockli, D.F., Planavsky, N.J., Lee, C.-T.A., 2016. Continental arc volcanism as the principal driver of icehouse-greenhouse variability. Science 352, 444–447.

Moynier, F., Chen, J., Zhang, K., Cai, H., Wang, Z., Jackson, M.G., Day, J.M., 2020. Chondritic mercury isotopic composition of Earth and evidence for evaporative equilibrium degassing during the formation of eucrites. Earth Planet. Sci. Lett. 551, 116544.

Nesbitt, H., Young, G., 1982. Early Proterozoic climates and plate motions inferred from major element chemistry of lutites. Nature 299, 715–717.

Percival, L.M., Bergquist, B.A., Mather, T.A., Sanei, H., 2021. Sedimentary mercury enrichments as a tracer of Large Igneous Province volcanism. In: Large Igneous Provinces: A Driver of Global Environmental and Biotic Changes, pp. 247–262.

Percival, L.M.E., Witt, M.L.I., Mather, T.A., Hermoso, M., Jenkyns, H.C., Hesselbo, S.P., Al-Suwaidi, A.H., Storm, M.S., Xu, W., Ruhl, M., 2015. Globally enhanced mercury deposition during the end-Pliensbachian extinction and toarcian OAE: a link to the karoo–Ferrar Large Igneous Province. Earth Planet. Sci. Lett. 428, 267–280.

Ravichandran, M., 2004. Interactions between mercury and dissolved organic matter–a review. Chemosphere 55, 319–331.

Sanei, H., Grasby, S.E., Beauchamp, B., 2011. Latest Permian mercury anomalies. Geology 40, 63–66.

Selin, N.E., 2009. Global biogeochemical cycling of mercury: a review. Annual Review of Environment and Resources 34, 43–63.

Shen, J., Algeo, T.J., Chen, J., Planavsky, N.J., Feng, Q., Yu, J., Liu, J., 2019. Mercury in marine Ordovician/Silurian boundary sections of South China is sulfide-hosted and non-volcanic in origin. Earth Planet. Sci. Lett. 511, 130–140.

Shen, J., Algeo, T.J., Hu, Q., Zhang, N., Zhou, L., Xia, W., Xie, S., Feng, Q., 2012. Negative C-isotope excursions at the Permian-Triassic boundary linked to volcanism. Geology 40, 963–966.

Shen, J., Feng, Q., Algeo, T.J., Liu, J., Zhou, C., Wei, W., Liu, J., Them, T.R., Gill, B.C., Chen, J., 2020. Sedimentary host phases of mercury (Hg) and implications for use of Hg as a volcanic proxy. Earth Planet. Sci. Lett. 543, 116333.

Štrok, M., Baya, P.A., Hintelmann, H., 2015. The mercury isotope composition of Arctic coastal seawater. C. R. Geosci. 347, 368–376.

Svensen, H.H., Frolov, S., Akhmanov, G.G., Polozov, A.G., Jerram, D.A., Shiganova, O.V., Melnikov, N.V., Iyer, K., Planke, S., 2018. Sills and gas generation in the Siberian traps. Philos. Trans. R. Soc. A, Math. Phys. Eng. Sci. 376, 20170080.

Wang, J., Li, Z.-X., 2003. History of Neoproterozoic rift basins in South China: implications for Rodinia break-up. Precambrian Res. 122, 141–158.

Wang, P., Du, Y., Yu, W., Algeo, T.J., Zhou, Q., Xu, Y., Qi, L., Yuan, L., Pan, W., 2020. The chemical index of alteration (CIA) as a proxy for climate change during glacial-interglacial transitions in Earth history. Earth-Sci. Rev. 201, 103032.

Wang, X., Cawood, P.A., Zhao, H., Zhao, L., Grasby, S.E., Chen, Z.-Q., Wignall, P.B., Lv, Z., Han, C., 2018. Mercury anomalies across the end Permian mass extinction in South China from shallow and deep water depositional environments. Earth Planet. Sci. Lett. 496, 159–167.

Yin, R., Feng, X., Chen, B., Zhang, J., Wang, W., Li, X., 2015. Identifying the sources and processes of mercury in subtropical estuarine and ocean sediments using Hg isotopic composition. Environ. Sci. Technol. 49, 1347–1355.

Yin, R., Feng, X., Wang, J., Bao, Z., Yu, B., Chen, J., 2013. Mercury isotope variations between bioavailable mercury fractions and total mercury in mercury contaminated soil in Wanshan Mercury Mine, SW China. Chem. Geol. 336, 80–86.

Yin, R., Krabbenhoft, D.P., Bergquist, B.A., Zheng, W., Lepak, R.F., Hurley, J.P., 2016. Effects of mercury and thallium concentrations on high precision determination of mercury isotopic composition by Neptune Plus multiple collector inductively coupled plasma mass spectrometry. J. Anal. At. Spectrom. 31, 2060–2068.

Zerkle, A.L., Yin, R., Chen, C., Li, X., Izon, G.J., Grasby, S.E., 2020. Anomalous fractionation of mercury isotopes in the Late Archean atmosphere. Nat. Commun. 11, 1–9.

Zhang, Q., Chu, X., Bahlburg, H., Feng, L., Dobrzinski, N., Zhang, T., 2003. Stratigraphic architecture of the Neoproterozoic glacial rocks in the "Xiang-Qian-Gui" region of the central Yangtze Block, South China. Prog. Nat. Sci. 13, 783–787.

Zhao, J.-H., Li, Q.-W., Liu, H., Wang, W., 2018. Neoproterozoic magmatism in the western and northern margins of the Yangtze Block (South China) controlled by slab subduction and subduction-transform-edge-propagator. Earth-Sci. Rev. 187, 1–18.

Zhou, C., Huyskens, M.H., Lang, X., Xiao, S., Yin, Q.-Z., 2019. Calibrating the terminations of Cryogenian global glaciations. Geology 47, 251–254.